JGR Space Physics

Key Points:

- TWINS ion spectra agree with RBSP in situ H^+ ion spectra during main phase of geomagnetic storms on March 17 and October 7, 2015
- O^+ ions contribute to peaks at energies 5–10 keV/amu in TWINS ion spectra which spatially extend to L < 5 and in the premidnight MLT sectors
- Spatial dynamics of TWINS ion spectra reveal signatures of varying convection rates, particle injections, and energy-dependent drift

Correspondence to:
S. Shekhar,
sap.shekh@gmail.com

TWINS Observations of the Dynamics of Ring Currents Ion Spectra on March 17 and October 7, 2015

S. Shekhar[1] ⓘ, J. D. Perez[1] ⓘ, and C. P. Ferradas[2,3] ⓘ

[1]Department of Physics, Auburn University, Auburn, AL, USA, [2]Geospace Physics Laboratory, NASA Goddard Space Flight Center, Greenbelt, MD, USA, [3]Department of Physics, Catholic University of America, Washington DC, USA

Abstract Direct comparisons between RBSP (Van Allen Probes or Radiation Belt Storm Probes) and TWINS (Two Wide-angle Imaging Neutral-atom Spectrometers) for the main phase of two storms, March 17 and October 7, 2015, showed agreement between the in situ ion measurements and the ion spectra from the deconvolved energetic neutral-atom (ENA) measurements, except when O^+ ions were significant. Spatial evolution of individual energy peaks in the ion spectra is studied using TWINS data. O^+ ions are seen to result in intense peaks at 5–10 keV/amu in the TWINS ion spectra. These ion populations are confined to low L shells (L < 5) and localized in the premidnight sector. When H^+ ions are significant, the low energy peaks (<25 keV/amu) are found to be less intense than the high energy peaks (>25 keV/amu), located at L > 4 and localized within the premidnight sector. During times of rapidly varying AE indices, two spatially distinct peaks, between 3–5R_E and 6–8R_E, are observed for the ions with energies >25 keV/amu. The outer peak appears for a few hours and fades while the inner peak is more stable. These structures are found to be consistent with particle injections observed in the RBSP data. When double peaked structures are swept off, low energy ions accumulate in the premidnight to midnight sectors whereas high energy ions are located premidnight to postmidnight sectors. Faster drift orbits of >25 keV/amu ions may cause this kind of distribution.

1. Introduction

Earth's magnetosphere is a highly dynamic region constantly interacting with particles emitted from the Sun. Processes such as trapping and energization of these particles contribute to the variability of space weather. Electrons and ions with energies less than 100 keV/amu are significant constituents of ring currents (RC) formed around Earth and contribute to several space weather effects due to the magnetic and electric fields produced and modified by it. Though mostly composed of ions, the contribution from electrons may be dependent on geomagnetic activity. A recent study of Van Allen Probe data has shown that the electrons contributed to almost 10% of the energy content of ions (Zhao et al., 2017). The transport of ions and electrons from the plasma sheet into the inner magnetosphere are known to be caused by magnetospheric convection due to the currentless eastward E×B drift from the large-scale electric fields induced by the solar wind (Axford, 1969). Energy and charge dependent gradient-curvature drift then put these particles in drift orbits forming the ring currents which can be symmetric or asymmetric depending on closed or open drift orbits of the ions, respectively.

In situ observations of RC by Smith and Hoffman (1974) on Explorer 45 first revealed "Nose-like", "wedge-like" or "trunk-like" ion spectral structures, named after their shapes as seen in energy-time spectrograms. These spectral RC ion structures were later confirmed in several other observations (Buzulukova et al., 2003, 2002; Dandouras et al., 2009; Ebihara et al., 2004; Ejiri et al., 1980; Ferradas et al., 2016b; Ganushkina et al., 2001; Lennartsson et al., 1979; Li et al., 2000; Peterson et al., 1998; Vallat et al., 2007; Zhang et al., 2015). Ion spectral nose structures are characterized by absence of certain ion energies and penetration of ions within a narrow energy range as observations are made from higher to lower L shells. The effects of the transport of the ions and electrons by convection and magnetic drift were first examined by Chen (1970) in order to explain the nose structure. They assumed a dawn-dusk electric field and calculated the plasma flow patterns for various magnetic moments and found that a forbidden region on the dusk side resulted from the corotation of the low-moment ions to the dawn side. Jaggi and Wolf (1973) demonstrated similar forbidden regions on the dusk side. Further, lower-moment protons would penetrate deeper into the magnetosphere until gradient drift and corotational forces were comparable. Ion nose structures would

hence be expected from convection theory (Smith & Hoffman, 1974). On the akebono satellite, ion nose structures were observed as monoenergetic ion dropoffs or ion spectral gaps were observed at ion energies ~10 keV. Drift path calculations by Shirai et al. (1997) showed that they were consistent with the previously mentioned forbidden regions. On INTERBALL, similar ion spectral gaps were observed by Kovrazhkin et al. (1999) and were attributed to magnetospheric residence times well above the ion lifetime.

Multinose structures (multiple ion spectral gaps) have also been observed by Polar (Ebihara et al., 2004; Li et al., 2000) and Cluster (Vallat et al., 2007). Ebihara et al. (2004) attributed these structures to changes in the convection electric field and changes in the distribution function of the source through particle trajectory tracings. Vallat et al. (2007) were able to reproduce single and double noses through particle trajectory tracings but found that the triple noses required a more complex electric field model. Through a case study of comparison of multiple-nose structures observed by the Helium, Oxygen, Proton, and Electron (HOPE) instrument on board Van Allen Probe A over one complete orbit on September 28, 2013 with an empirical electric field model, Ferradas et al. (2016a) found that nose structures showed signatures of ion drift in the highly dynamic environment of the inner magnetosphere, consistent with Ebihara et al. (2004).

In a recent study by Ferradas et al. (2016b), Van Allen Probes data were used to statistically investigate the nose structures for the ion species H^+, He^+, and O^+. They found that multiple-nose events occur mostly in heavy ions and during quiet times. Further, the occurrence probabilities of single nose (single energy peaked-ion spectra) increased with increasing activity levels while double nose (two energies peaked-ion spectra) were more common during quiet times. Such in situ observations provide a localized view, however, energetic neutral atoms (ENA) imagers like TWINS can be used to observe the global RC dynamics. The ENA imaging of storm-time ring currents was first shown by Roelof (1987) using ISEE one measurements. Since then, several studies such as those by Polar (Henderson et al., 1997), Astrid (Barabash et al., 1997), IMAGE (Burch et al., 2001), and TWINS (Two Wide-angle Imaging Neutral-atom Spectrometers) (Goldstein & McComas, 2013), were conducted where ENA imaging was performed to understand magnetospheric RC dynamics.

Previous studies such as those by Perez et al. (2015, 2012) have provided a better understanding of ion energy spectra obtained from TWINS. Perez et al. (2012) showed the presence of non-Maxwellian features in the TWINS ion energy spectra. They observed a primary maximum in the 15–20 keV/amu range below which the ion flux was Maxwellian. Sometimes, they also observed a second component with a maximum in the 40–50 keV/amu range occurring at the beginning of the recovery phase of a storm in agreement with in situ THEMIS observations. Further, Perez et al. (2016) found 30 keV/amu ion flux and pressure anisotropies obtained from TWINS in agreement with RBSPICE observations for a geomagnetic storm on March 17, 2015. Recent cross-scale observations by Goldstein et al. (2017) involving THEMIS, Van Allen Probes, and TWINS, studied the variations in the spatial, spectral, and temporal structure of the same storm and found agreement between their ion spectra. While TWINS ion spectra have shown agreement with in situ data, the association between "nose-like" ring current ion spectra observed by Ferradas et al. (2016b) and two peaked-ion spectra observed on TWINS remain unexplored.

The objectives of this study are twofold, (1) comparison between "nose-like" ring current ion spectra observed by Ferradas et al. (2016b) and two peaked-ion spectra observed on TWINS and (2) a study of the spatial and temporal evolution of individual nose energy ion populations. In section 2, we describe the TWINS and Van Allen Probes dataset, moving on to section 3, where we compared Van Allen Probes H^+ spectra with TWINS ion spectra and studied the dynamics of the geomagnetic storms on March 17 and October 7, 2015. The summary is presented in section 4.

2. Datasets Used

2.1. TWINS (Two Wide-angle Imaging Neutral-Atom Spectrometers)

NASA TWINS are a pair of identical imagers in two widely separated Molniya orbits with inclinations of 63.4°, perigee altitudes of ~1,000 km, and apogees in the Northern Hemisphere at ~7.2 RE. Each spacecraft is three-axis stabilized and approximately nadir pointing and provides nearly continuous coverage of

magnetospheric energetic neutral-atom (ENA) emissions, over a broad energy range (1–100 keV/amu) with high angular (4° × 4°) and time (about 1 min) resolution.

Electrons from the atoms in the neutral exosphere, through charge exchange collisions with energetic ions, lead to the creation of energetic neutral atoms. Since these neutrals escape the geomagnetic field, they can be measured remotely by the ENA imagers and are used to reconstruct the global equatorial ion distribution as elaborated in Appendix A of Perez et al. (2012). There can be two sources of near-Earth ENA emissions: (1) High altitude emissions (HAE) and (2) Low altitude emissions (LAE) (Roelof, 1997). The HAEs are optically thin emissions formed in single collision and charge exchange interactions. These are generated when magnetospheric plasma undergoes charge exchange with cold neutral hydrogen from the geocorona and provide information regarding ring current and/or plasma sheet dynamics. The LAEs are often the brightest emissions in ENA images especially early in a geomagnetic storm (Valek et al., 2010) and are produced by the multiple-collision interaction of precipitating energetic ions with the atomic oxygen exosphere at altitudes of a few to several hundred kilometers. They are optically thick and their origin is in particles mirroring near the Earth with local pitch angles close to 90° (Bazell et al., 2010).

To construct a full image, each TWINS instrument has sensor heads that are mounted together on a rotating actuator, which sweeps back and forth, scanning 180° in 1 min and then taking 22 s to orient in the opposite direction roughly over an Earth-centered viewing cone, scanning 180° in another 1 min (Goldstein & McComas, 2013). A detailed descriptions of TWINS instruments are given in McComas et al. (2009). The ENA images used in this study are centered at ion energies (E_{cen}) from 5 to 65 keV/amu in 5 keV/amu steps (i.e., 13 energy channels) integrated over $[\frac{E_{cen}}{2}, \frac{3E_{cen}}{2}]$ to obtain statistically significant ion fluxes. Hence, ENA flux at a central energy of 65 keV/amu is flux integrated over energies of 32.5–97.5 keV/amu. Typical ENA images at some energies are shown in Figures 1a–1h and 2a–2j.

In this study, we have used the equatorial ion distributions integrated over all pitch angles obtained from TWINS ENA images through a deconvolution technique explained in Appendix A of Perez et al. (2012). TWINS determines ion energies based on ENA velocities (Perez et al., 2012) and the ion species composition can be determined using the pulse height distribution using a technique similar to that described by Mitchell et al. (2003) and Valek et al. (2013, 2015). Valek et al. (2018) found that during the main phase of the March 17, 2015 storm, O^+/H^+ ratio rose to a notably high value of ~1. However, the deconvolution of O^+ ions is complex, especially when the interaction at low altitudes is considered (LAEs). Hence, deconvolutions were performed on the total ENA signal. To obtain the ion energy spectra, the ENA images centered at ion energies (E_{cen}) were used. From the deconvolved ion intensities observed by TWINS, a singular value decomposition (SVD) fit was obtained. The energy spectrum that when integrated and properly weighted with the energy-dependent charge exchange cross section, resembles the SVD fit, is taken to be physical energy spectrum. The method is explained in detail in Appendix B of Perez et al. (2012). Figures 1i and 2k show sample spectra (green) resulting from SVD fit (red) with the actual equatorial ENA intensities integrated over all pitch angles (blue). The energy spectra mostly have a primary maximum in the 10–20 keV/amu range and a second peak in the 30–50 keV/amu energy range which was also demonstrated by Perez et al. (2015) for two time periods, May 29, 2010, 13:30–14:30 UT and May 26, 2011, 16:45–17:15 UT.

2.2. RBSP (Radiation Belt Storm Probe) or Van Allen Probe

NASA's Van Allen Probes or Radiation Belt Storm Probes are a network of two identical spacecraft (RBSP A and B) launched in August 2012. The satellites are in a highly elliptical, near-equatorial (10° inclination) orbit with perigee at 1.1 RE, apogee at 5.8 RE, orbital period of ~9h, and a spin period of ~11s. The preigee-apogee line precesses in local time at a rate of ~210° per year. Both satellites carry Helium Oxygen Proton Electron (HOPE) mass spectrometer (Funsten et al., 2013) which measures both ions and electrons over the ~1 to ~50 keV/amu energy range. The measurements are made in five angular directions coplanar with the spacecraft spin axis and 72 energy channels with energy resolution $\Delta E/E \sim 15\%$. It also uses a spherical electrostatic analyzer and a time-of-flight mass spectrometer with channel electron multiplier detectors to distinguish between the magnetospheric ion species (H^+, He^+, and O^+). The detectors are designed to
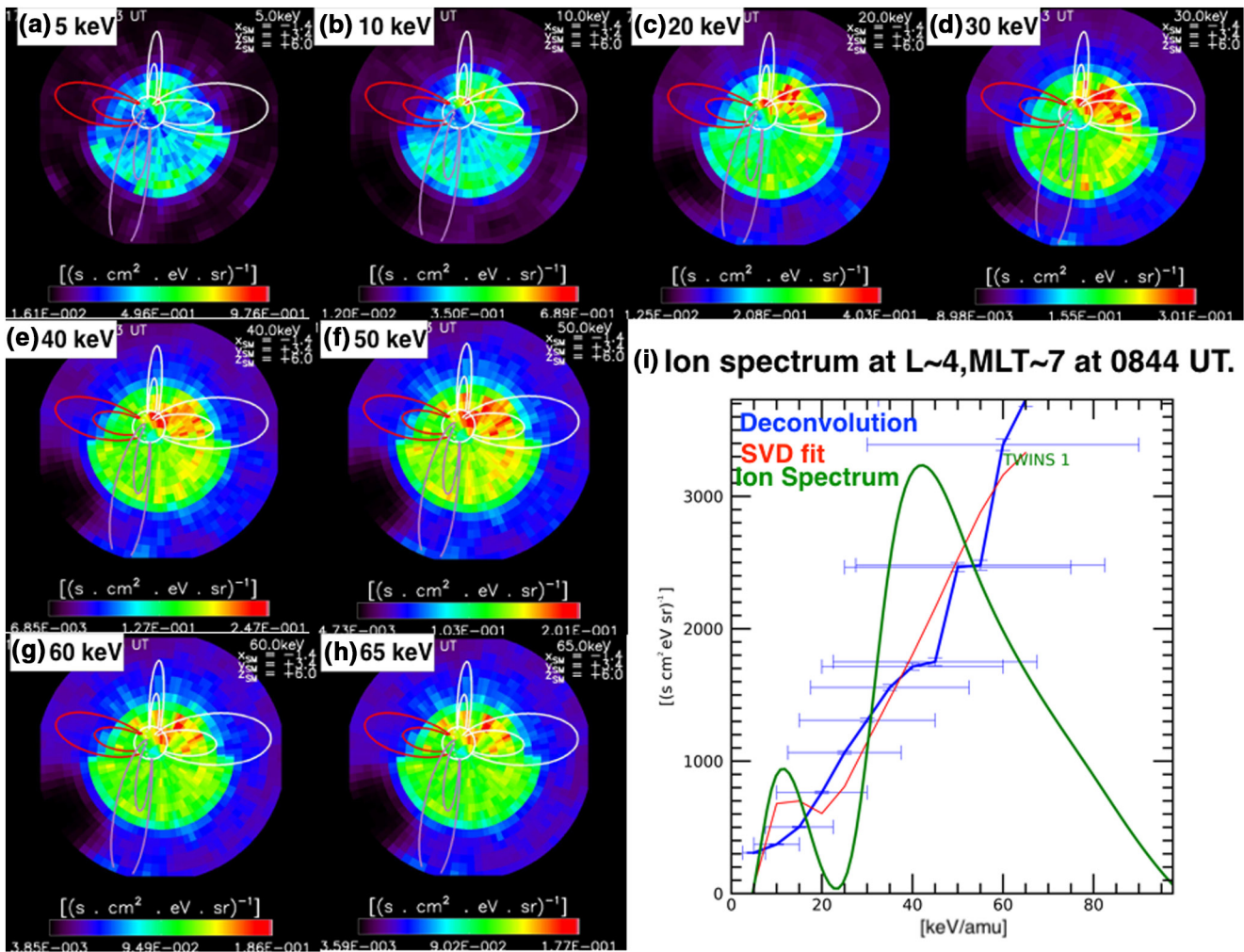
Figure 1. (a–h) ENA images from TWINS on a skymap projection with dipole field lines plotted at McIlwain L shells, L = 4 and 8 RE at 08:44 UT on March 17, 2015. The images are integrated over 15–16 sweeps corresponding to ~15 m of observation time. The red and purple L shells point in the sun and dusk directions, respectively. (i) Deconvolved ion intensities integrated over pitch angles and energy bands given by the x error bars are plotted in Blue. The energy spectrum that when integrated and properly weighted with the energy-dependent charge exchange cross section, resembles the SVD fit shown in red, is taken to be physical energy spectrum and is shown in green. ENA, energetic neutral atom; TWINS, Two Wide-angle Imaging Neutral-atom Spectrometers; SVD, singular value decomposition.

operate in the harsh environment of the Earth's radiation belts through minimal contamination due to penetrating relativistic particles.

3. Observations

The observations of each geomagnetic storm (March 17 and October 7, 2015) studied includes two parts, one is the comparison and validation of TWINS ion spectra with RBSP H^+ ion spectra, and second is the study of RC spatial dynamics using TWINS data alone. The spatial dynamics of TWINS ion spectra were studied at certain times picked to account for the varying geomagnetic conditions through varying solar wind parameters such as IMF Bz and By, solar wind speed, AE index, and Sym/H, the quality of images obtained from TWINS and whether deconvolution could be successfully performed. We captured the spatial distribution of the two ion nose peaks during times of varying convection rates through changing IMF Bz directions, time varying By and rapidly varying AE index indicative of particle injections. We picked two storms to account for the variations in TWINS data due to the contributions of O^+ ions. While on March 17,
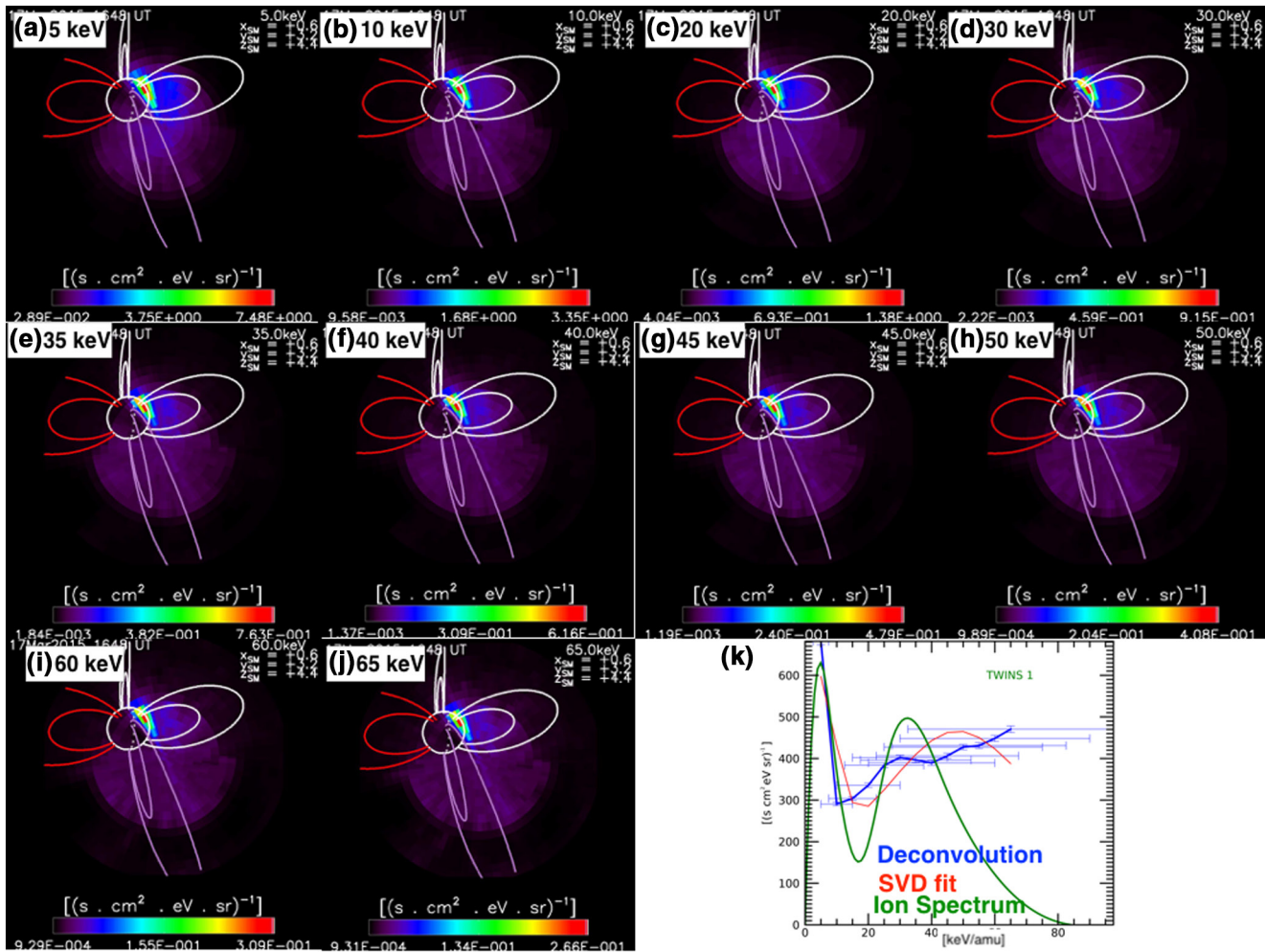
Figure 2. (a–j) Same as Figure 1 for 16:40 UT on March 17, 2015. (k) Same as 1i at L ~ 3.3 and MLT ~18 on 16:40 UT on March 17, 2015.

O^+ ions were comparable to H^+ ions during the main phase, on October 7, O^+ ions were almost 100 times less intense than H^+ ions.

3.1. March 17, 2015

3.1.1. Geomagnetic Conditions

The solar wind conditions and RBSP ion (H^+, He^+, O^+) flux data on March 17, 2015 are shown inFigures 3 and 4, respectively. We used RBSP HOPE data to observe the ion spectra on the day. RBSP A and B were located in the dusk-midnight-morning sectors between 05:00 and 23:00 UT. Figure 4 shows the H^+, He^+, and O^+ intensities from RBSP A (left) and B (right), respectively, for the entire day. The times at which RBSP spectra were compared with TWINS in Figures 5 and 6 are marked by vertical lines and labeled from a to g. The vertical lines marked from a to i in Figure 3 correspond to times at which TWINS RC spatial dynamics were studied in Figures 7 and 8.

At 05:13 UT, IMF By and Bz were positive, solar wind speed increased rapidly, AE index was flat and Sym/H was positive indicating geomagnetically quiet conditions (marked as time a in Figure 3). Around 05:20 UT, By turned negative while Bz was still positive until 06:00 UT when Sym/H starts dipping to negative values marking the beginning of the main phase of the geomagnetic storm. RBSP B observed two ion nose structures in the H^+ ion spectra (marked as time a in right plot in Figure 4). Note that He^+ and O^+ are much less intense than H^+ ions at this time.
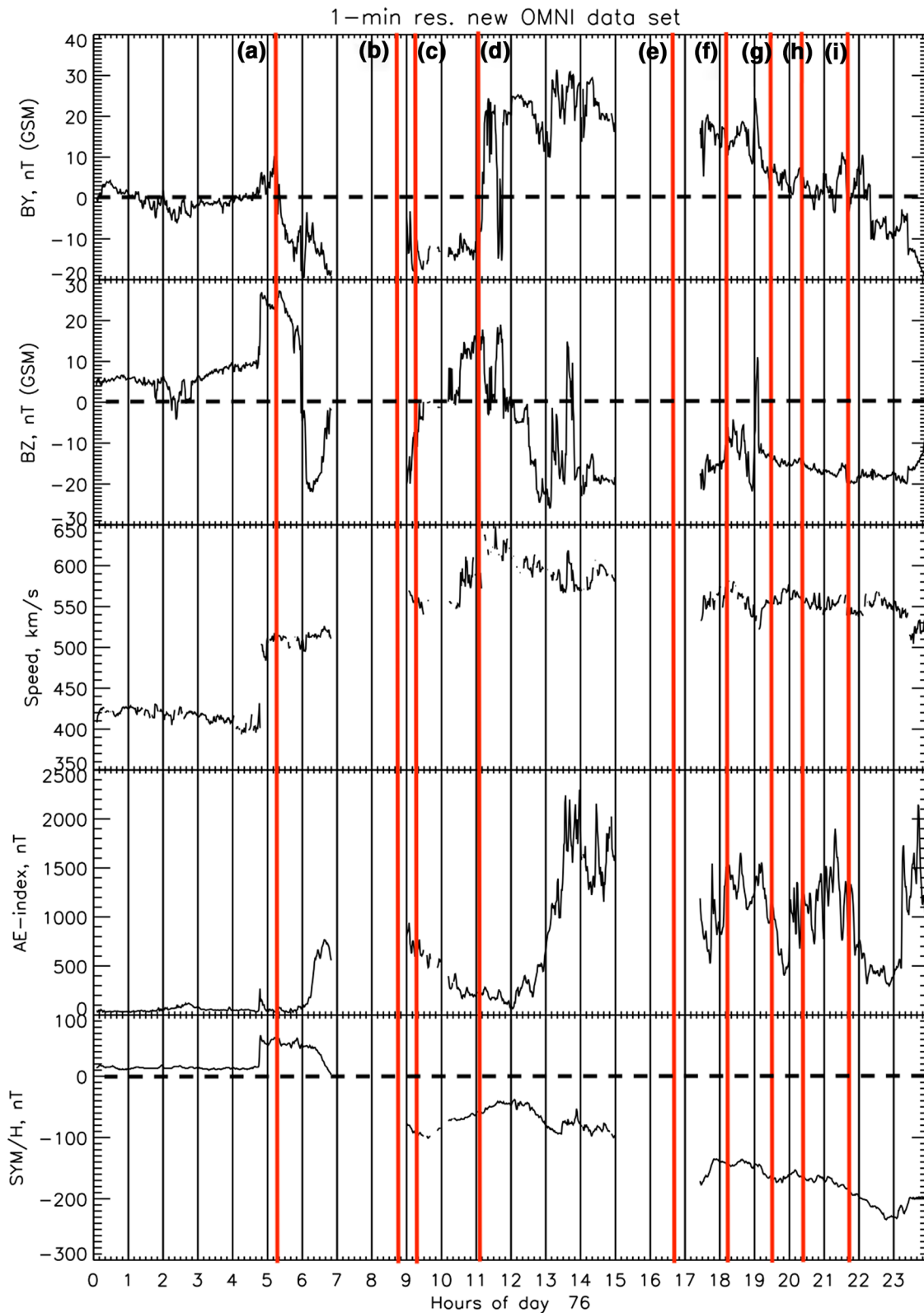
Figure 3. Solar wind data on March 17, 2015. The times at which spatial dynamics of ion spectra peak energies were studied are marked in red and labeled as (a) 05:13 UT, (b) 08:44 UT, (c) 09:14 UT, (d) 10:59 UT, (e) 16:40 UT, (f) 18:14 UT, (g) 19:29 UT, (h) 20:14 UT, and (i) 21:44 UT.
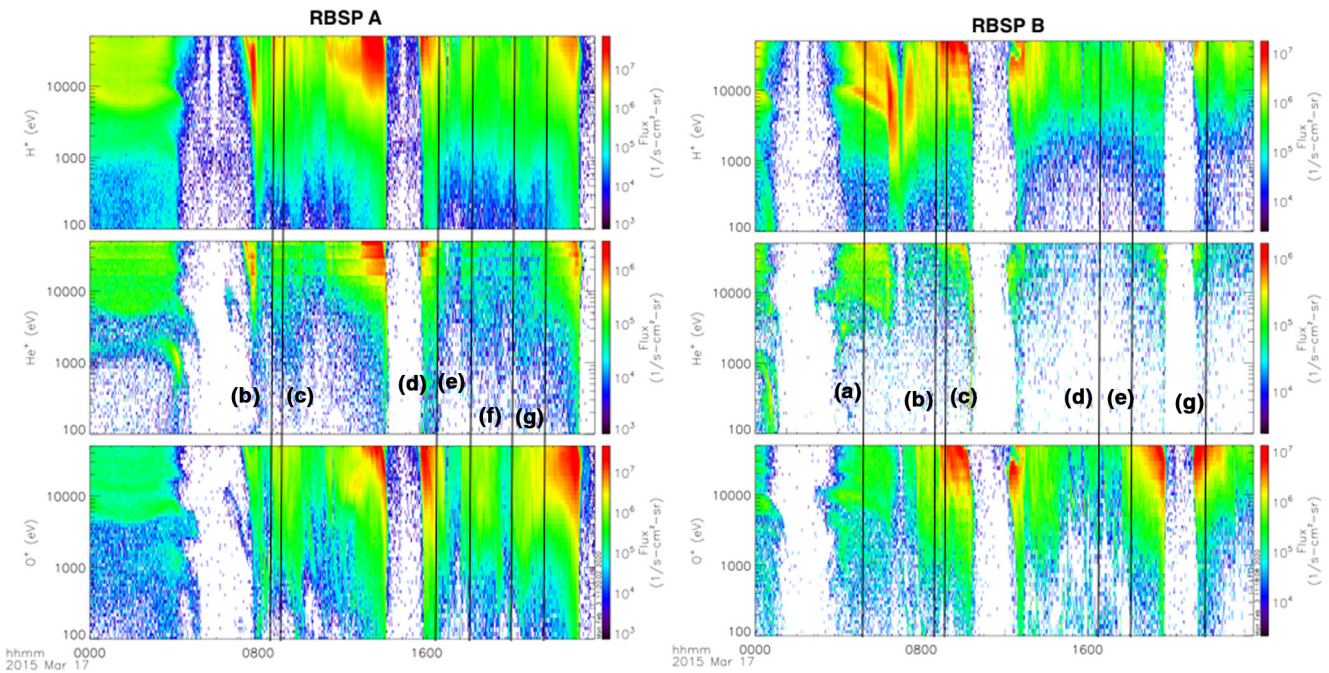
Figure 4. H^+, He^+, and O^+ ion intensities (top to bottom) from RBSP A (left) and B (right), respectively, for the entire day on March 17, 2015. The times at which RBSP H^+ spectra were compared with TWINS are marked by vertical lines and labeled as (a) 05:13 UT, (b) 08:44 UT, (c) 09:14 UT, (d) 16:40 UT, (e) 18:14 UT, (f) 20:14 UT, and (g) 21:44 UT. RBSP, Radiation Belt Storm Probes. TWINS, Two Wide-angle Imaging Neutral-atom Spectrometers.

Between 08:44 and 09:14 UT (marked as times b and c in both plots in Figures 4 and 3), IMF By and Bz were negative, solar wind speed did not vary much from a, some fluctuations were seen in the AE index and Sym/H dipped to ~ -100 nT. This indicates that convection rates had increased and more ions from the plasmasheet were injected into the inner magnetosphere. Both RBSP A and B were located in the ring current region (L $\sim$ 3–8) and the two-nose structure was not as prominent as at 05:13 UT. Around 09:14 UT (marked as time c in both plots in Figure 4), o^+ ions have become comparable to H^+ ions consistent with fresh O^+ ion injections.

At 10:59 UT (marked as time d in Figure 3), IMF Bz turned positive while By remained negative indicating that convection rates had slowed down from 09:14 UT. The AE index was again flat and Sym/H recovered to ~ -70 nT consistent with slowing of convection. Between 11:00 and 13:00 UT, IMF Bz again turned southward and RBSP A which was in the ring current region observed a sharp increase in all the ion intensities (see left plot in Figure 4, between times c and d) supporting enhanced plasma transport from the plasmasheet.

Rapid fluctuations in the AE index were seen from 13:00 UT till the end of the day (Figure 3). TWINS data were found to be extremely noisy from 13:00to 16:40 UT. Hence, we started our observations from 16:40 UT (marked as time e in Figure 3), where the AE index peaked and Sym/H dipped to ~ -120 nT indicating that more ions were injected. IMF Bz continued to stay southward for the rest of the day and AE index showed rapid fluctuations implying enhanced convection and ion injections. Certain times were picked after 16:40 UT (marked as times f–i in Figure 3) to examine the injections in detail through TWINS spatial ion distributions to be done in later Sections. For the times (d) 16:40 UT, (e) 18:14 UT, (f) 20:14 UT, and (g) 21:44 UT shown in Figure 4, o^+ ions are found to be comparable to H^+ ions which is consistent with enhanced convective transport from a plasma sheet richer in plasma from an ionospheric source.
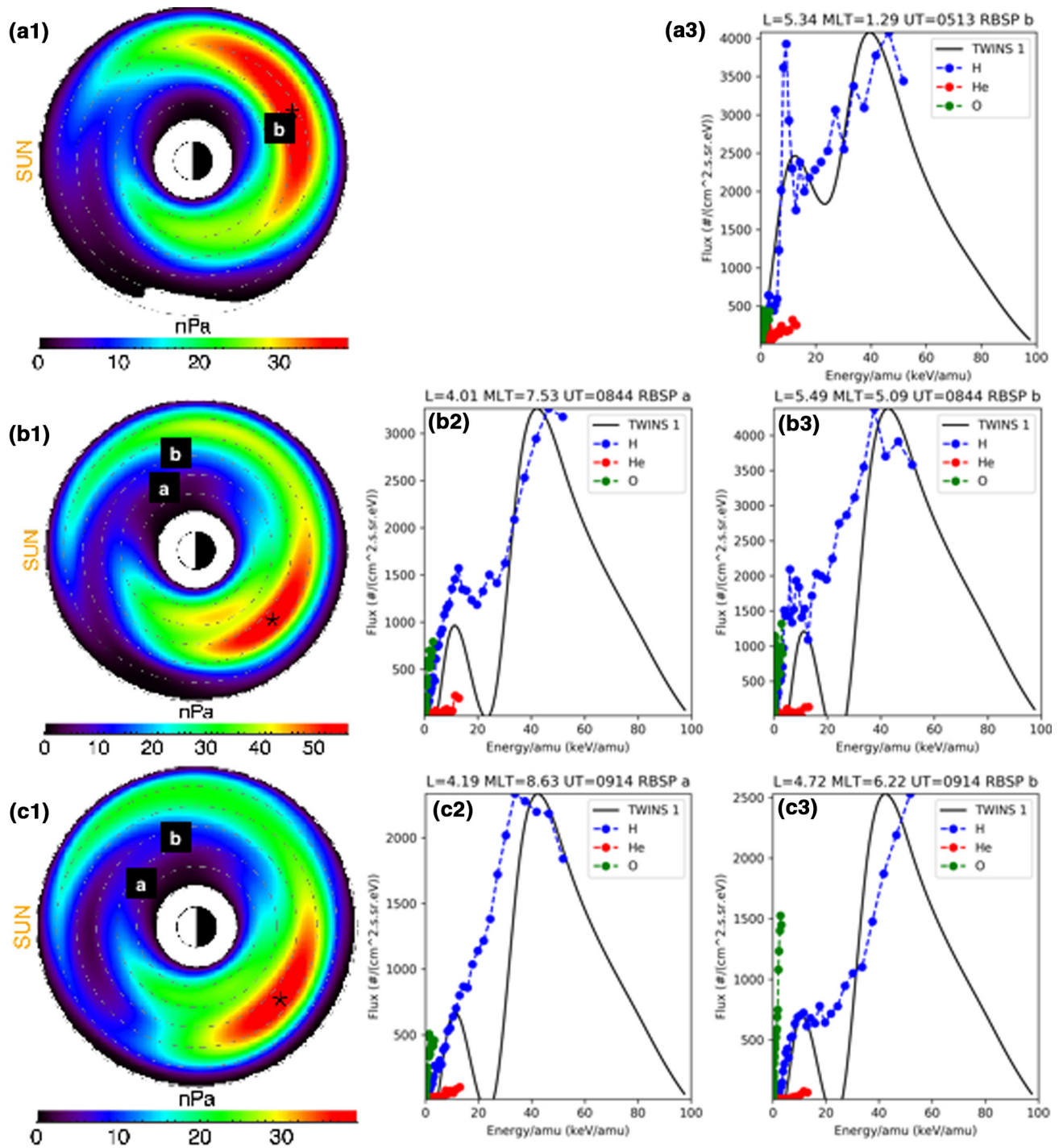
Figure 5. (a.1–c.1) The locations of RBSP A and B on TWINS ion pressure distributions at 05:13, 08:44, and 09:14 UT, respectively. Sun is to the left. Black star shows the location of ion pressure peak. These were quiet times and O$^+$ intensities were ~100 times lower than H$^+$. (a.2–c.2) Spectra obtained from TWINS and RBSP A and (a.3–c.3) spectra obtained from TWINS and RBSP B for the same times on March 17, 2015. Both RBSP A and B H$^+$ ion fluxes were roughly 10^4 times greater than TWINS for all time periods on this day and were rescaled to TWINS maximum ion flux (Scaling factor ~10^{-4}). The plot rows correspond to the times marked in Figure 4. RBSP, Radiation Belt Storm Probes. TWINS, Two Wide-angle Imaging Neutral-atom Spectrometers.
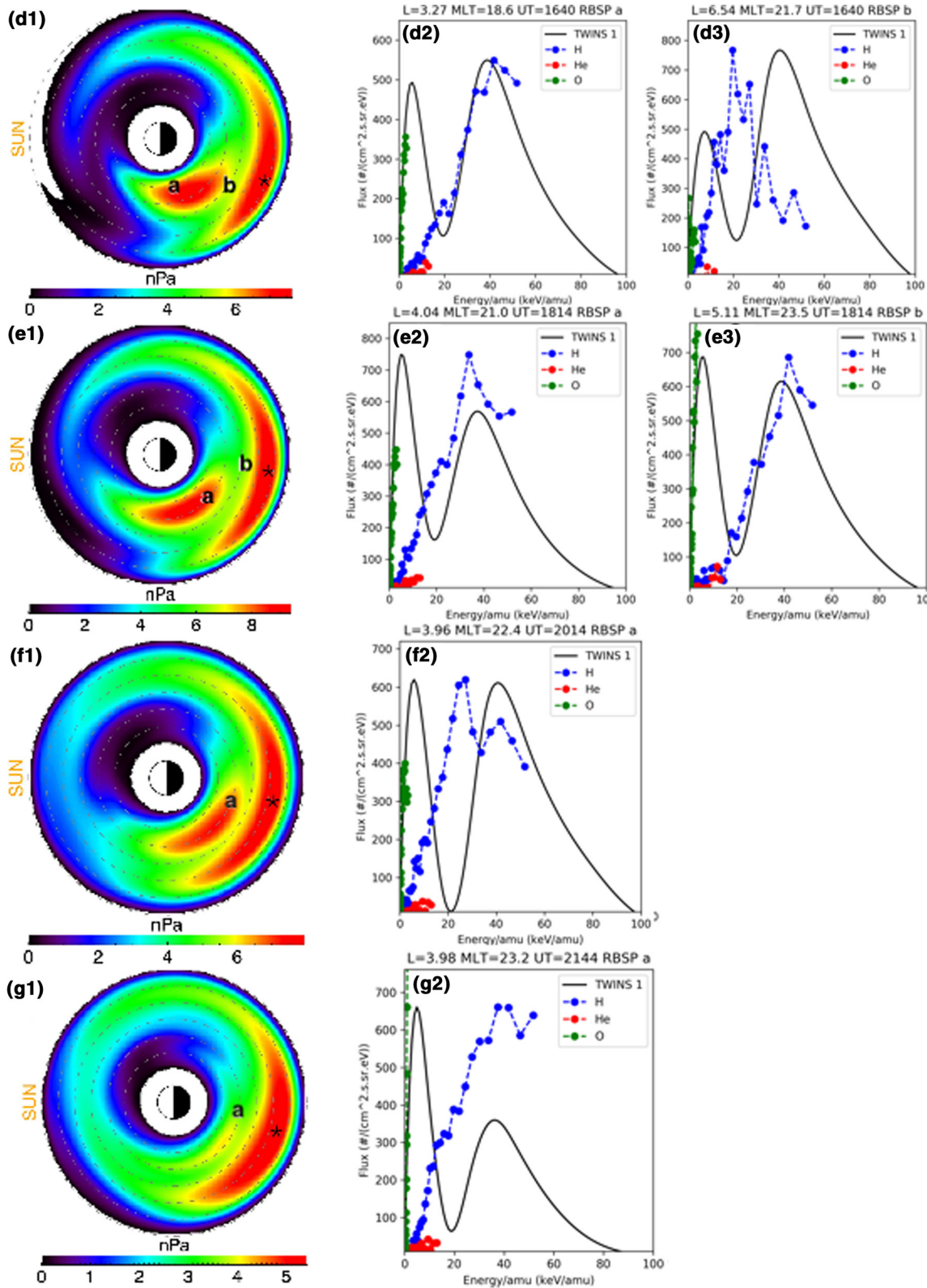
Figure 6. (d.1–g.1) The locations of RBSP A and B on TWINS ion pressure distributions at 16:40, 18:14, 20:14, and 21:44 UT, respectively. Sun is to the left. Black star shows the location of ion pressure peak. These were active times and O^+ intensities were comparable to H^+. (d.2–g.2) Spectra obtained from TWINS and RBSP A and (d.3–g.3) spectra obtained from TWINS and RBSP B for the same times on March 17, 2015. Both RBSP A and B H^+ ion fluxes were roughly 10^4 times greater than TWINS for all time periods on this day and were rescaled to TWINS maximum ion flux (Scaling factor ~10^{-4}). The plot rows correspond to the times marked in Figure 4. RBSP, Radiation Belt Storm Probes. TWINS, Two Wide-angle Imaging Neutral-atom Spectrometers.
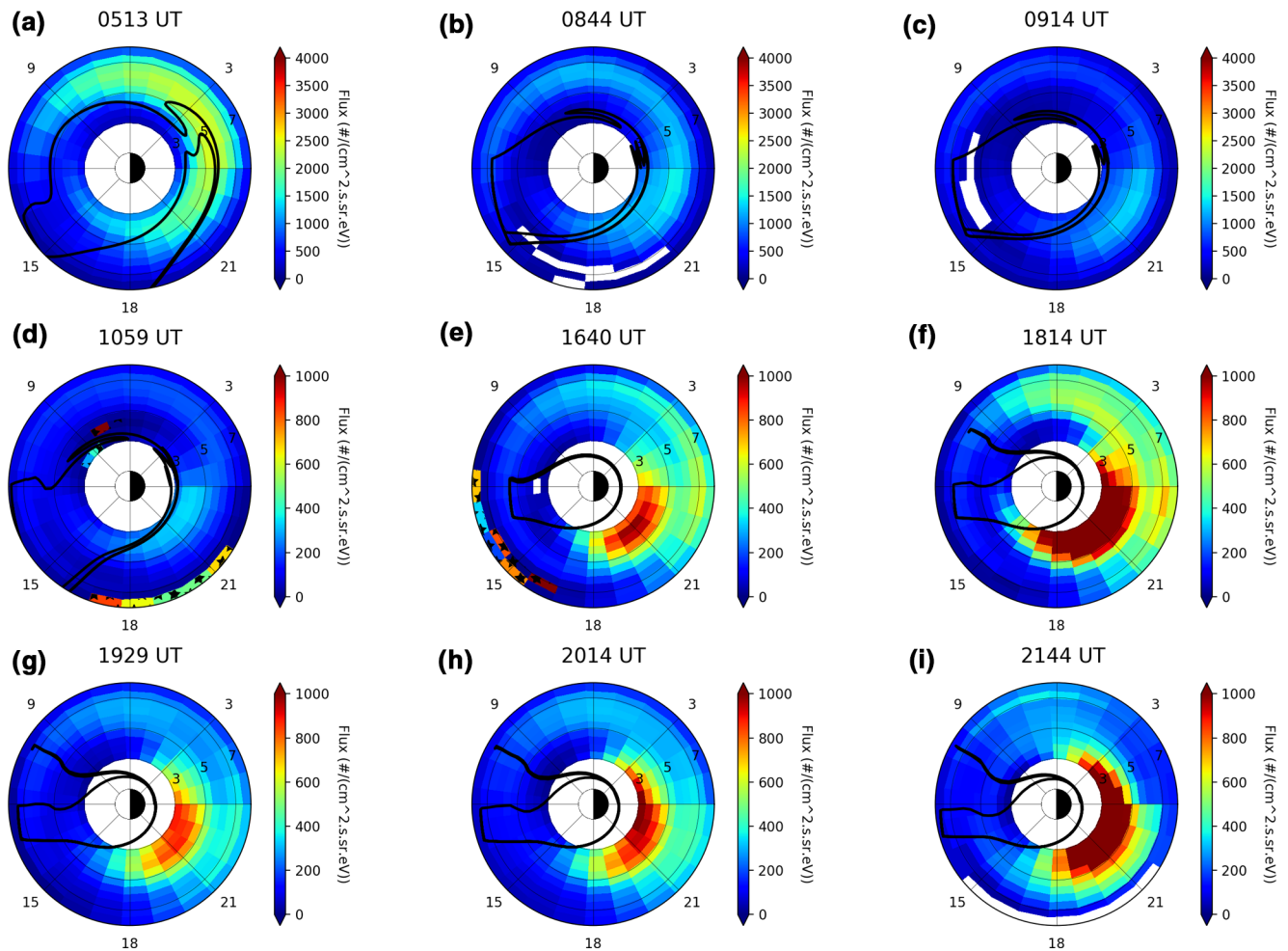
Figure 7. (a–i) Spatial distribution of ion intensities for ion energy peaks <25 keV/amu at the labeled times on March 17, 2015. Sun is located to the left. The ion spectra peaks were observed at L shell increments of 0.5 from L = 3 and MLT increments of 1. The black stars mark the locations at which the ENA pixel signal was too weak for deconvolution to be successful. The plasmasphere boundary obtained through plasmapause test particle (PTP) simulation model of Goldstein et al. (2014) is overplotted in black. ENA, energetic neutral atom.

3.1.2. Comparison of TWINS Ion Spectra With RBSP Observations

RBSP spectra observations were compared with TWINS obtained spectra at times for which ENA fluxes were significant enough so that deconvolution and SVD could be successfully done to obtain ion spectra. Figure 5 shows ion spectra obtained from TWINS at locations of RBSP A and B at 05:13, 08:44 and 09:14 UT plotted over ion pressure plots obtained from TWINS. The ion pressure data were integrated over the energy range 2.5–97.5 keV/amu (Perez et al., 2012).

In order to emphasize the relative spatial and temporal behavior of the RBSP H$^+$ and TWINS ion fluxes, the RBSP H$^+$ fluxes are rescaled using equation (1) so that the maximum flux in from each source is the same. For March 17, the scaling factor ($\frac{F_{maxtwins}}{F_{maxrbsp}}$) was determined to be ~$10^{-4}$.

$$F_{rbspnew} = \frac{F_{rbsp} \cdot F_{maxtwins}}{F_{maxrbsp}} \qquad (1)$$

For H$^+$ ions in RBSP, $F_{rbspnew}$ is the rescaled flux, F_{rbsp} is the observed flux, $F_{maxrbsp}$ is the maximum flux observed in RBSP for that species and $F_{maxtwins}$ is the maximum ion flux observed in TWINS. Also, RBSP spectra are reported in ion energies of keV and were converted to keV/amu to compare with TWINS ion spectra. Hence, if 48 keV O$^+$ ions were observed, they were reported as 48 keV/16 amu ~3 keV/amu ions.
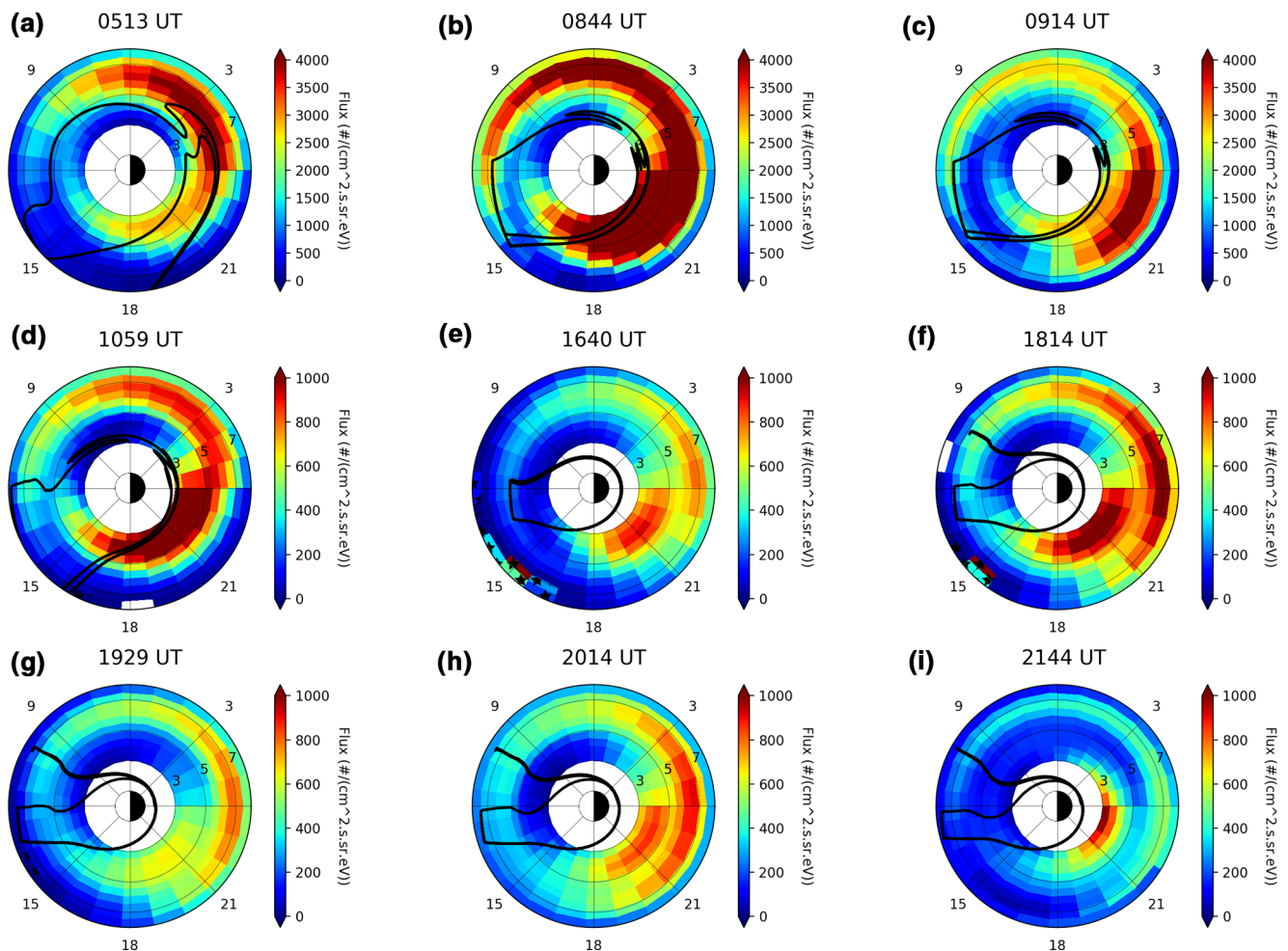
Figure 8. (a–i) Spatial distribution of ion intensities for ion energy peaks >25 keV/amu at the labeled times on March 17, 2015. Sun is located to the left. The ion spectra peaks were observed at L shell increments of 0.5 from L = 3 and MLT increments of 1. The black stars mark the locations at which the ENA pixel signal was too weak for deconvolution to be successful. The plasmasphere boundary obtained through plasmapause test particle (PTP) simulation model of Goldstein et al. (2014) is overplotted in black. ENA, energetic neutral atom.

The question of the lack of agreement between the absolute magnitude fluxes in situ and ENA-derived measurements has been discussed in several cases: (1) Vallat et al. (2004) compared Cluster-CIS (Escoubet et al., 1997) and IMAGE-HENA (Mitchell et al., 2000) observations, and found that for weak flux values the inversion method applied to IMAGE-HENA systematically overestimated the ion flux values (factor of 32) with respect to the CODIF ones, (2) Perez et al. (2012) compared THEMIS ESA (McFadden et al., 2008) and SST (Angelopoulos, 2008) spectral measurements with TWINS during a CIR storm on July 22, 2009, (3) Grimes et al. (2013) compared TWINS and THEMIS ion spectra during the May 29, 2010 geomagnetic storm and found that the TWINS ion fluxes were almost 3 times lower than in situ fluxes from THEMIS, (4) Perez et al. (2016) compared RBSPICE-A and TWINS during a CME storm on March 17, 2015, and (5) Goldstein et al. (2017) found differences among THEMIS, RBSPICE (Radiation Belt Storm Probes Ion Composition Experiment) ion spectra and TWINS results. While TWINS ion fluxes were found to be almost 50 times smaller than RBSPICE, RBSP HOPE H^+ fluxes were found to be >20 times that of RBSPICE which are two different instruments on the same spacecraft. We found that RBSP HOPE H^+ fluxes were roughly 10^4 times greater than TWINS which are in agreement with Goldstein et al. (2017) observations on March 17, 2015. The disagreement between TWINS and in situ measurements can be partially explained by the fundamental difference between in situ versus ENA-derived global flux. TWINS measured ENA flux includes contributions from along a given line of sight (LOS) through the distribution of ENA emission sources thus representing the average emission from a source volume. This could lead to blurring of fine structures and

flux extremes resulting in the ENA-derived ion flux at a given location being lower than the in situ measured values. For a thorough discussion of possible explanations for the differences in absolute values, see Goldstein et al. (2017).

The plot rows in Figure 5 correspond to the times marked in Figure 4. Row a in Figure 5 corresponds to the time marked as a (5:13 UT) in Figure 4. RBSP B was located at an L ~ 5 and on the postmidnight sector (MLT ~ 1 h) close to the maximum pressure peak (Figure 5a.1) and the corresponding H^+ spectra was found to be in agreement with TWINS observations with peak intensities at energies ~13 and ~37 keV/amu (Figure 5a.3). This trend continues with ~ 13 keV/amu ion peak diminishing with time at 08:44 UT (Figures 5b.2 and 5b.3) and 09:14 UT (Figures 5c.2 and 5c.3) where both RBSP A and B were located away from the pressure peaks (Figures 5b.1 and 5c.1).

Between 13:00 and 15:00 UT, Bz was negative and AE index increased rapidly indicating that there were fresh injections of ions from the plasmasheet due to increased convection. RBSP A and B were located in the premidnight sector close to the pressure maxima which had moved duskward (Figures 6d.1, e.1, f.1, and g.1). Further, multiple pressure peaks were observed in TWINS data. At all these times post 16:00 UT, a very low energy peak (5–10 keV/amu) was observed in TWINS ion spectra missing in RBSP H^+ ion spectra (Figures 6d.2, 6d.3, 6e.2, 6e.3, 6f.2, 6f.3, 6g.2, and 6g.3). However, as stated previously, RBSP observed O^+ ion intensities to be comparable with H^+ which may have resulted in the low energy peak in TWINS as the total ENA signal was deconvolved. The low energy peak obtained in TWINS data when O^+ ions are comparable may have been a result of ion energies calculated through velocity measurements of O^+ ions with the assumption of H^+ ions. Hence, if an ion peak was observed in TWINS at 5 keV/amu, it may have been a result of 16 amu × 5 keV/amu = 80 keV O^+ ions since O^+ ions are 16 times heavier than H^+ ion.

3.1.3. Dynamics of Individual Ion Energy Peaks (<25 keV/amu and >25 keV/amu)

We investigated the spatial and temporal evolution of ion populations belonging to each of the ion energies at which peaks were obtained. As stated in previous Sections, double energy peaks were observed by TWINS at all times with one peak at energies <25 keV/amu and other at >25 keV/amu. Hence, we studied the two energies separately. In order to compare our observations with the results obtained by (Goldstein et al., 2017), we studied the RC ion distributions relative to the plasmasphere boundary obtained through plasmapause test particle (PTP) simulation model of Goldstein et al. (2014) which assumes that the time–variable, global plasmapause boundary is an ensemble of E×B drifting test particles. Figures 7 and 8 show the L-MLT distribution of ion populations belonging to energies <25 keV/amu and >25 keV/amu, respectively. During deconvolution, sum of normalized chi-squared and a penalty function from Wahba (1990) is minimized to fit the ENA data and obtain a smooth solution, respectively (Perez et al., 2012). The black stars mark the regions where a good fit to the ENA data could not be found (high chi-square or penalty function) resulting in inaccurate observations of ion spectra through SVD.

Spatial distributions of low energy peak (<25 keV/amu) intensities are shown in Figure 7 and high energy peak (>25 keV/amu) intensities are shown in Figure 8. The spatial distributions at 05:13, 08:44, and 09:14 UT (Figures 7a–7c) show initial asymmetric RC extending from 18 to 09 h in MLT at 05:13 UT and then slowly accumulating ions on the premidnight sector at 09:14 UT. At 05:13 UT, it was geomagnetically quiet and AE index was flat so the ion distributions may have been due the remnant ion populations. As seen in Figures 8a–8c, the distributions of >25 keV/amu ion distributions between 05:13 and 10:59 UT are very similar to the <25 keV/amu energy ion distributions.

Figures 7a and 8a show that at 05:13 UT, the double-nose structures were present all around the region of corotating, partially depleted cold plasma. At 0605 UT, southward turning Bz enhanced convection and a steep increase in RC ion flux (~50%) was observed for the >25 keV/amu ion populations whereas the < 25 keV/amu ion fluxes depleted at 08:44 UT compared to 05:13 UT (Figures 8 and 7b). Between 09:14 and 10:59 UT, both ion energy populations in the RC mostly decay accumulating in the pre–midnight sector (Figures 8c and 8d and 7c and 7d). After ~1300 UT, when rapid fluctuations in the AE index accompanied by southward turning IMF Bz were observed, a major buildup of the midnight sector ring current (Figure 8e) was initiated. TWINS observations of the evolution of the storm are in agreement with Goldstein et al. (2017) where a similar evolution was observed through in situ data.

Further, TWINS observations show that sustained convection after ~1300 UT shifted the dusk side partial RC to lower L shells (L < 4) (Compare partial dusk side RC populations in Figures 8e–8i; and 7e and 7i) for both ion energies while before 13:00 UT, it was located at L > 5. The TWINS flux increases from 16:40 UT (Figures 7e–7i) supports enhanced ion transport of <25 keV/amu ions (5–10 keV/amu peaks) which correspond to O^+ ions. It indicates that these distributions may have been a result of O^+ ions as they will penetrate deeper in the magnetosphere (Ferradas et al., 2016a).

Globally, the higher energy ions were found to be more dynamic than the low energy ion distributions. At 16:40 UT (Figure 8d), two spatially separated ion intensity peaks are observed. The inner high energy spatial ion peak remains constant while the outer one appears at the postmidnight MLT sectors at 16:40 UT (Figure 8d) and then gradually expands eastward into the premidnight sector until 20:14 UT (Figures 8e–8g), then fades away around 21:44 UT (Figure 8h). They are correlated with rapid fluctuations in the AE index from 13:00 to 22:00 UT, indicative of convective intermittent injections of >25 keV/amu ions.

3.2. October 7, 2015

3.2.1. Geomagnetic Conditions

Figure 9 shows the solar wind data on October 7, 2015. The commencement of storm began around 03:30 UT and the Sym/H index was negative throughout. At around 03:30 UT, the Sym/H index dips to more negative values down to −80 nT at 09:00 UT and a second dip is observed at a minimum of −120 nT around 22:30 UT. IMF Bz remains negative from 3:30 to 9:30 UT and fluctuates between positive and negative values until 22:00 UT. A lot of fluctuation is observed in the AE index while the solar wind speed stays ~400 km/s until 14:00 UT increasing to 800 km/s by the end of the day. Figure 10 shows the RBSP ion (H^+, He^+, O^+) flux data on October 7, 2015. At 2:00 UT (marked as a in Figures 9 and 10), the geomagnetic conditions were quiet and RBSP B observed double peaked H^+ ion spectra. Note that He^+ and O^+ are almost 100 times less than H^+ ions in intensity. Enhanced convection is observed a few hours before 05:00 UT (marked as b in Figures 9 and 10) as IMF Bz turns southward, RBSP A shows a faint low energy peak (~15 keV/amu) and a relatively intense high energy peak (>30 keV/amu) while RBSP B shows single-nose H^+ ion spectra. At 11:00 UT where recovery from the first Sym/H dip was observed and 21:00 UT, which was 1 hour before the second Sym/H dip (marked as e and i in Figures 9c and 9d in Figure 10), single-nose ion spectra were observed.

3.2.2. Comparison of TWINS Ion Spectra With RBSP Observations

At 02:00 UT on October 7, 2015, RBSP B was located in the noon sector (Figures 11a.1). Though the fluxes in TWINS are low at noon, we still found a good agreement between RBSP B and TWINS ion spectra. RBSP A was at perigee. RBSP B observed a double peaked H^+ ion spectrum which was also observed by TWINS (Figures 11a.3). This was a relatively quiet time with Sym/H ~ −20 nT and IMF Bz nearly 0. Figures 11b.2 and 11b.3 show TWINS and RBSP A and B ion spectra on 05:00 UT which were located in the postnoon sector (Figures 11b.1). RBSP A was at L < 5, and observed an H^+ spectrum with a small low energy peak and a large peak at 40 keV/amu which was in agreement with TWINS. RBSP B was at L > 5, and the low energy (<25 keV/amu) peak was observed as a tiny bump whereas TWINS did not observe much variation from the ion spectrum at L < 5. This is not surprising as the resolution of in–situ measurements are expected to be better (Figures 11b.2 and 11b.3). RBSP A and B were in the noon sector at 11:00 UT and 21:00 UT (Figures 11c.1 and 11d.1). The ion spectra were found to mostly have single nose at ~40 keV/amu and agreed with TWINS ion spectra (Figure 11c.3). At 21:00 UT (Figures 11d.2 and 11d.3) both RBSP and TWINS observed a peaked-ion spectra with peaks at energies between 40 and 50 keV/amu and a bump on tail at around 13 keV/amu.

3.2.3. Dynamics of Individual Ion Energy Peaks (<25 keV/amu and >25 keV/amu)

Figures 12 and 13 show the spatial and temporal dynamics of ion populations belonging to the ion peak at energy <25 keV/amu and >25 keV/amu, respectively, at the labeled times on October 7, 2015. Plasmapause boundaries from PTP simulation model are overplotted and were in general contracted on this day. Between 2:00 and 05:00 UT, little variation was observed in the AE index and IMF Bz turned southward around 03:30 UT (Figure 9). The >25 keV/amu ion flux between 2:00 and 05:00 UT increased slightly (seeFigures 13a and 13b) around midnight sector while <25 keV/amu ion populations decreased in flux (see Figures 12a and 12b).
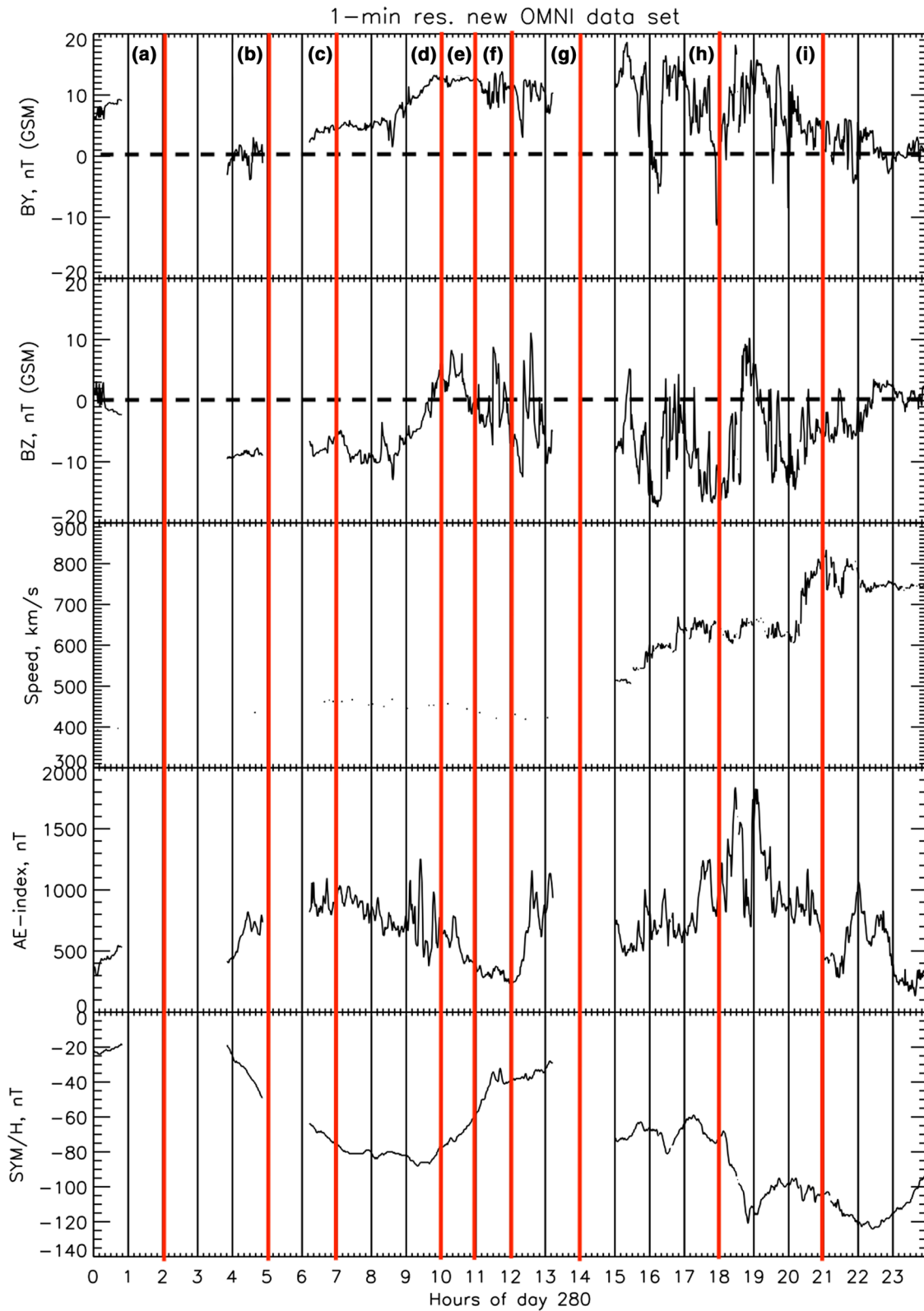
Figure 9. Solar Wind data on October 7, 2015. The times at which spatial dynamics of ion spectra peak energies were studied are marked in red and labeled as (a) 02:00 UT, (b) 05:00 UT), (c) 07:00 UT, (d) 10:00 UT, (e) 11:00 UT, (f) 12:00 UT, (g) 14:00 UT, (h) 18:00 UT, and (i) 21:00 UT.
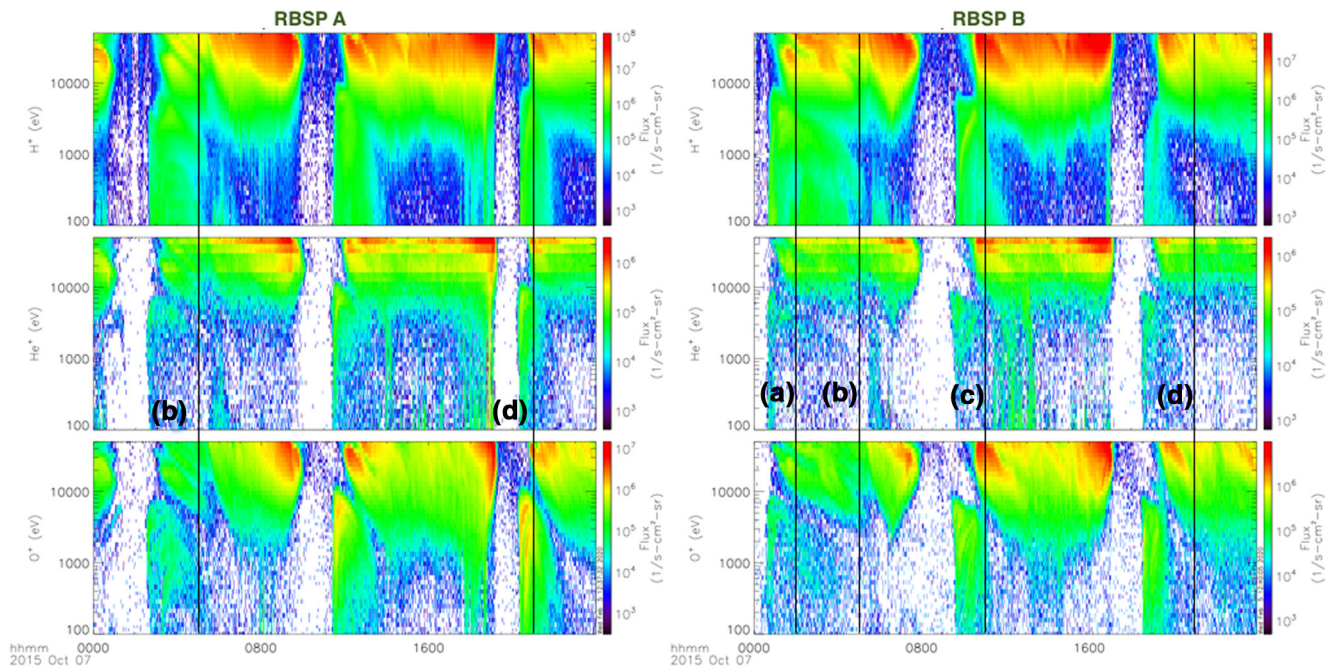
Figure 10. H$^+$, He$^+$, and O$^+$ ion intensities (top to bottom) from RBSP A (left) and B (right), respectively, for the entire day on October 7, 2015. The times at which RBSP H$^+$ spectra were compared with TWINS are marked by vertical lines and labeled as (a) 02:00 UT, (b) 05:00 UT, (c) 11:00 UT, and (d) 21:00 UT. RBSP, Radiation Belt Storm Probes. TWINS, Two Wide-angle Imaging Neutral-atom Spectrometers.

Around 07:00 UT, sustained convection which began at 03:30 UT further enhanced ion intensities for both the nose energies in TWINS data and an increase in the <25 keV/amu energy ion fluxes accumulating in the premidnight sector was observed (Figures 12c and 13c). As IMF Bz turned northward again at 09:30 UT, slowing the convection rate, ion fluxes were found to steadily decrease between 10:00 and 12:00 UT as seen in Figures 12d–12f and 13d–13f. At these times, spatial profiles of ion intensities in the two energy ranges (>and <25 keV/amu) revealed that at some locations double peaked-ion spectra changed to single peaked and ions with the high energy ions localized themselves in the postmidnight sector (Figures 13e and 13f) whereas low energy ions were located in the premidnight sector (Figures 12e and 12f). This may have been due to the faster azimuthal drift of higher energy ions drifting westward from the premidnight to postmidnight sector.

From 14:00 UT, <25 keV/amu ion fluxes were very low (<200 cm^{-2} sr^{-1} s^{-1} eV^{-1}) (Figures 12g–12i). IMF Bz turned southward between 14:00 and 15:00 UT while the solar wind speed started increasing. The effect of enhanced convection is seen as a slight increase in the ion flux in the premidnight sector along the plasmapause boundaries in Figure 13g. At 18:00 (Figure 13h), two spatial peaks were observed in the high energy ion distribution in the premidnight sector, one between L ∼ 4–5, and another one at L ∼ 6–7. These structures occur again at times of high and rapidly varying AE index indicating intermittent ion injections. However, these were located at L > 4 contrary to the intermittent structures observed in the March 17 storm which extended to L < 4. Further, the solar wind speed was increasing steeply from 400–800 km/s as the Sym/H index was approaching its second dip. At 21:00 UT, RC intensity was found to be low but >25 keV/ amu ion distributions were more symmetric.

4. Conclusions and Future Work

We investigated the dynamics of ion spectra from TWINS for the main phase of two geomagnetic storms: March 17, 2015 (minimum Sym/H ∼200 nT) and October 7, 2015 (minimum Sym/H ∼120 nT). TWINS ion spectra were obtained through deconvolution of ENA images to obtain equatorial ion distributions followed by SVD solution with the best fit to the ion intensities at 13 energy bands between 2.5 and 97.5 keV/amu. The obtained ion spectra were validated through comparisons with RBSP HOPE H$^+$ ion spectra and global dynamics of the individual peaks in the ion nose spectra were explored with TWINS.
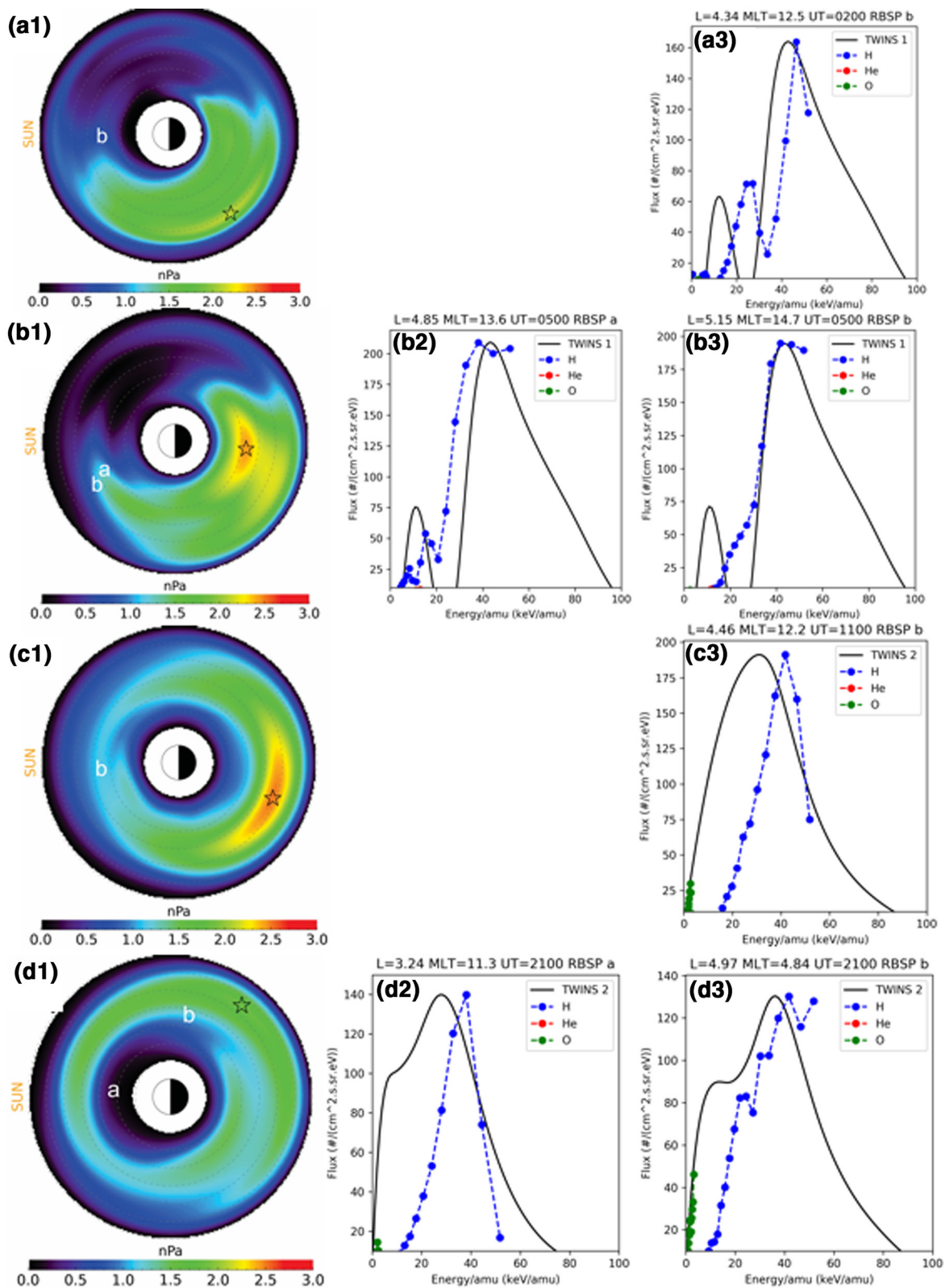
Figure 11. a.1—day.1 shows the locations of RBSP A and B on TWINS ion pressure distributions at 02:00, 05:00, 11:00, and 21:00 UT, respectively. Black star marks the location of the ion pressure peak. Sun is to the left. O$^+$ intensities were ~100 times lower than H$^+$. a.2—days.2 shows spectra obtained from TWINS and RBSP A and a.3—days.3 show spectra obtained from TWINS and RBSP B for the same times on October 7, 2015. Both RBSP A and B H$^+$ ion fluxes were roughly 10^5 times greater than TWINS for all time periods on this day and were rescaled to TWINS maximum ion flux (Scaling factor ~10^{-5}). RBSP, Radiation Belt Storm Probes. TWINS, Two Wide-angle Imaging Neutral-atom Spectrometers.
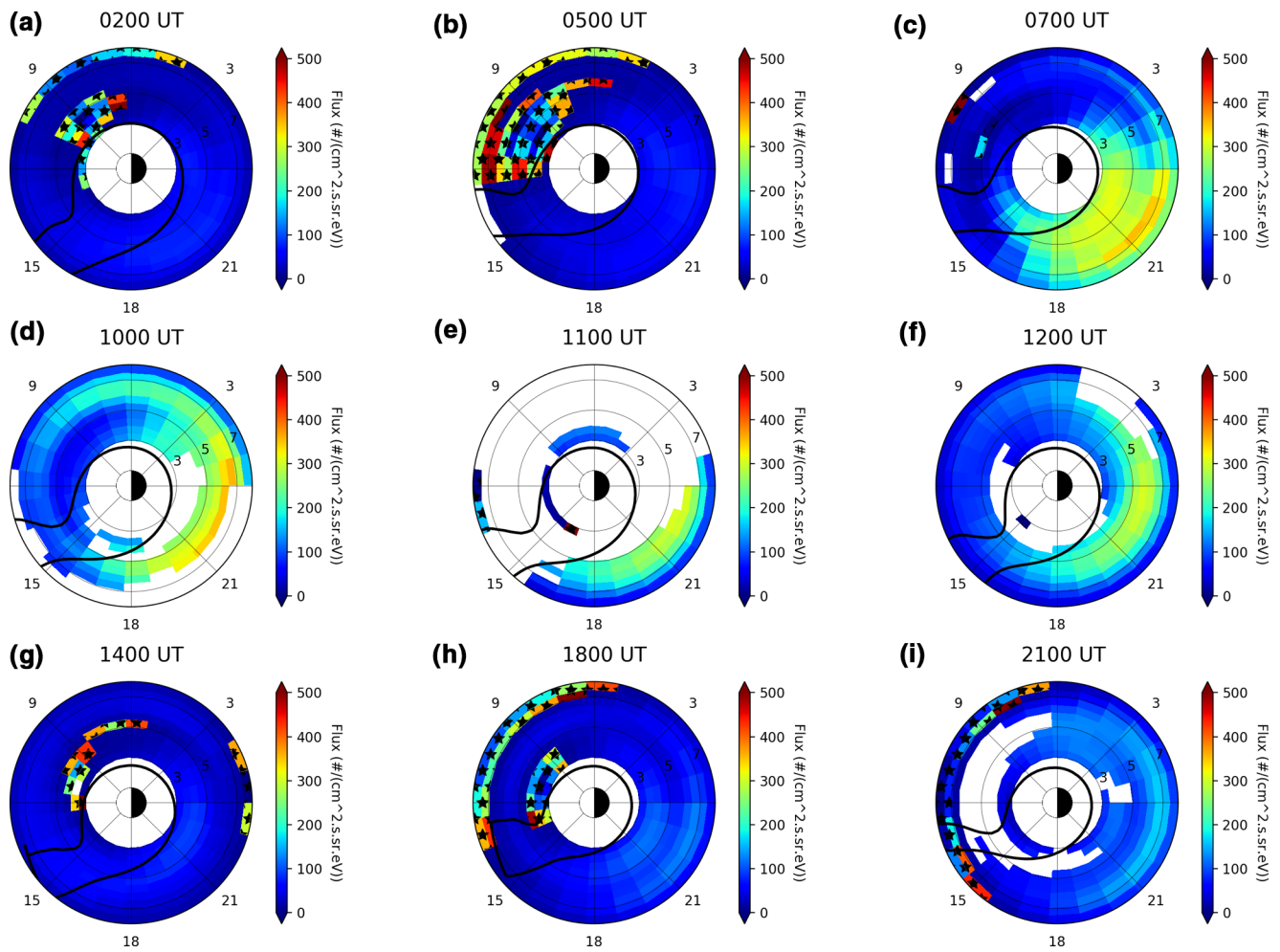
Figure 12. (a–i) Spatial distribution of ion intensities for ion energy peaks <25 keV/amu at the labeled times on October 7, 2015. Sun is located to the left. The ion spectra peaks were observed at L shell increments of 0.5 from L = 3 and MLT increments of 1. The black stars mark the locations at which the ENA pixel signal was too weak for deconvolution to be successful. The white areas above L = 3 are due to the absence of ion peaks in the energy range <25 keV/amu. The plasmasphere boundary obtained through plasmapause test particle (PTP) simulation model of Goldstein et al. (2014) is overplotted in brown. ENA, energetic neutral atom.

1. Nose-like structures have been previously observed in several in situ observations. In this study, TWINS double peaked spectra were found to have similarities with RBSP in situ H^+ ion spectra, except when O^+ ions were significant. This is not surprising as the total ENA signal was deconvolved for TWINS and the ion energies were obtained in keV/amu without any O^+ and He^+ ions distinctions. Therefore, the low energy peak obtained in TWINS data when O^+ contributions are comparable to H^+ ions are most likely to be a result of ion energies/amu calculated through velocity measurements of O^+ ions. Hence, if an ion peak was observed in TWINS at 5 keV/amu, it may have been a result of 16 amu × 5 keV/amu = 80 keV O^+ ions

2. We also studied the spatial and temporal variation of the two ion energy bands, one at energies <25 keV/amu and another at energies >25 keV/amu, individually. The low energy peaks (<25 keV/amu) were found to be less intense than the high energy peaks (>25 keV/amu) and localized within the premidnight sector during geomagnetically active times

3. Spatially, O^+ ions will penetrate to lower L shells (L < 5) which was also observed in the TWINS data during times when O^+ ions were significant. When H^+ ions were significant, low energy ions were mostly located at L > 5

4. During quite times, the ions in both the energy bands arranged themselves to form an asymmetric ring current system with ions fluxes lowest around prenoon and postnoon sectors. According to recent
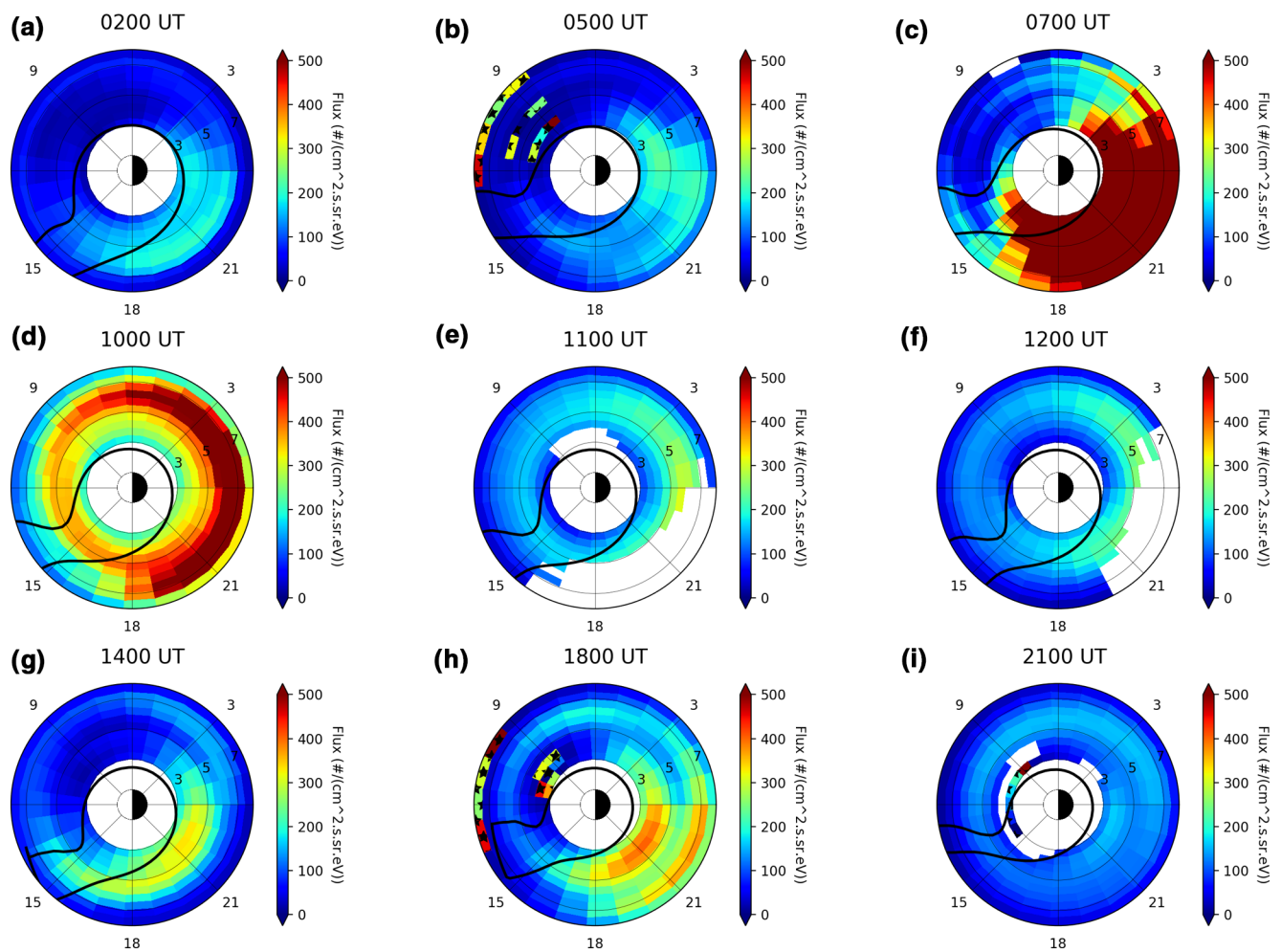
Figure 13. (a)–i) Spatial distribution of ion intensities for ion energy peaks >25 keV/amu at the labeled times on October 7, 2015. Sun is located to the left. The ion spectra peaks were observed at L shell increments of 0.5 from L = 3 and MLT increments of 1. The black stars mark the locations at which the ENA pixel signal was too weak for deconvolution to be successful. The white areas above L = 3 are due to the absence of ion peaks in the energy range >25 keV/amu. The plasmasphere boundary obtained through plasmapause test particle (PTP) simulation model of Goldstein et al. (2014) is overplotted in brown. ENA, energetic neutral atom.

cross-scale observations of the March 17, 2015 storm by Goldstein et al. (2017) involving THEMIS, Van Allen Probes, and TWINS, quiet double-nose proton spectra were observed in the region of corotating cold plasma which were in agreement with the spatial ion intensities data in TWINS (Figures 7a and 8a)

5. During times of rapidly varying AE indices, on March 17, between 16:40 UT to 20:14 UT and on October 7, at 18:00 UT, two spatial peaks were observed for the ions with energies >25 keV/amu. The inner and outer spatial peaks were located between 3 and 5 R_E and 6–8 R_E, respectively, on the pre to post midnight sectors. The outer peak appeared for a few hours and faded while the inner peak was more stable

6. On October 7, between 10:00 and 12:00 UT, at several locations, single-nose ion energy spectra were obtained. At this time IMF Bz had turned northward which may have resulted in slowing down of convection. The ions with energies <25 keV/amu accumulated around pre–midnight to midnight sectors whereas ions with energies >25 keV/amu were located pre to post midnight sectors. Faster drift orbits of >25 keV/amu ions may have led to this kind of distribution

Both the storms examined in this study demonstrate that double-nose structures are more common during quiet times while single-nose structures are more common during geomagnetically active times. This is in agreement with previous studies by Li et al. (2000), Vallat et al. (2007), and Ferradas et al. (2016b). Energies of ions injected were mostly found to be >25 keV which drifted into the morning sector within a few hours

while the low energy ion populations remained mostly in the premidnight sector. This suggests that multiple-nose structures are likely formed after long drifts from the magnetotail into the inner magnetosphere. Conclusion six directly shows that energy-dependent drift of ring current ions affects the spatial distribution of nose energies. We also observed that heavy ions like O^+ penetrated deeper into the magnetosphere, usually below L $\sim$5. This is somewhat consistent with a study by Lundin et al. (1980) using PROGNOZ-7 spacecraft, where it was shown that the heavy ions were significant inside the L $\sim$4 boundary while H^+ ions were often significant outside. Similar results were also obtained by Ferradas et al. (2015) using Cluster Ion Spectrometry (CIS)/COmposition DIstribution Function (CODIF) instrument onboard Cluster Spacecraft and Ferradas et al. (2016b) using Van Allen Probes data. Based on 2 years of Van Allen probes observations, Li et al. (2020) found that higher occurrences of single-nose structures were between 13 and 03 MLT whereas double-nose structures occurred mostly between 03 and 13 MLT. Our observations from October 7 storm are in agreement with this whereas such a trend was not observed for the March 17 storm.

During both the storms, we also observed spatial ion peaks for ion energies >25 keV/amu. Conclusion five shows that these spatial structures are correlated with high and rapidly varying AE indices. This indicates that these spatial structures may have been due to intermittent substorm injections. This has also been shown in a study by Perez et al. (2016) for the March 17 storm.

While Goldstein et al. (2017) compared TWINS data to in situ measurements, in our study we found that TWINS spatial data alone was able to capture these features as well as the differences in the evolution of RC ion populations in two different nose energy bands. Hence, it could be used to study the spatial and temporal evolution of different nose energies individually which could not be achieved through in situ measurements only. This work paves the way toward understanding of the global dynamics of the ion energy bands through TWINS observations. In future, similar case studies of more storms and comparison with RC models will be crucial toward understanding of the RC ion dynamics.

Data Availability Statement

All RBSP-ECT data are publicly available at the Web site http://www.RBSP-ect.lanl.gov/. PTP simulations are available at https://enarc.space.swri.edu/PTP/(October 7, 2015 PTP data attached as supp_info.zip in SI as website is undergoing maintenance).

References

Angelopoulos, V. (2008). The THEMIS mission. *Space Science Reviews*, *141*, 5–34. https://doi.org/10.1007/s11214-008-9336-1

Axford, W. I. (1969). Magnetospheric convection. *Reviews od Geophysics*, *7*, 421–459. https://doi.org/10.1029/RG007i001p00421

Barabash, S., Cson Brandt, P., Norberg, O., Lundin, R., Roelof, E. C., Chase, C. J., & Koskinen, H. (1997). Energetic neutral atom imaging by the Astrid microsatellite. *Advances in Space Research*, *20*, 1055. https://doi.org/10.1016/S0273-1177(97)00560-7

Bazell, D., Roelof, E. C., Sotirelis, T., Brandt, P. C., Nair, H., Valek, P., & McComas, D. (2010). Comparison of TWINS images of low-altitude emission of energetic neutral atoms with DMSP precipitating ion fluxes. *Journal of Geophysical Research*, *115*, A10204. https://doi.org/10.1029/2010JA015644

Burch, J. L., Mende, S. B., Mitchell, D. G., Moore, T. E., Pollock, C. J., Reinisch, B. W., & Reiff, P. H. (2001). Views of earth's magnetosphere with the IMAGE satellite. *Science*, *291*(5504), 619–624. https://doi.org/10.1126/science.291.5504.619

Buzulukova, N. Y., Galperin, Y. I., Kovrazhkin, R. A., Glazunov, A. L., Vladimirova, G. A., Stenuit, H., & Delcourt, D. C. (2002). Two types of ion spectral gaps in the quiet inner magnetosphere: Interball-2 observations and modeling. *Annales Geophysicae*, *20*, 349–364. https://doi.org/10.5194/angeo-20-349-2002

Buzulukova, N. Y., Kovrazhkin, R. A., Glazunov, A. L., Sauvaud, J. A., Ganushkina, N. Y., & Pulkkinen, T. I. (2003). Stationary nose structures of protons in the inner magnetosphere: Observations by the ION instrument onboard the Interball-2 satellite and modeling. *Cosmic Research*, *41*, 3–12. https://doi.org/10.1023/A:1022343327565

Chen, A. J. (1970). Penetration of low-energy protons deep into the magnetosphere. *Journal of Geophysical Research*, *75*, 2458–2467. https://doi.org/10.1029/ja075i013p02458

Dandouras, I., Cao, J., & Vallat, C. (2009). Energetic ion dynamics of the inner magnetosphere revealed in coordinated Cluster-Double Star observations. *Journal of Geophysical Research*, *114*, A01S90. https://doi.org/10.1029/2007JA012757

Ebihara, Y., Ejiri, M., Nilsson, H., Sandahl, I., Grande, M., Fennell, J. F., & Fritz, T. A. (2004). Multiple discrete-energy ion features in the inner magnetosphere: 9 February 1998, event. *Annales Geophysicae*, *22*, 1297–1304. https://doi.org/10.5194/angeo-22-1297-2004

Ejiri, M., Hoffman, R., & Smith, P. H. (1980). Energetic particle penetrations into the inner magnetosphere. *Journal of Geophysical Research*, *85*, 653–663. https://doi.org/10.1029/ja085ia02p00653

Escoubet, C. P., Schmidt, R., & Goldstein, M. L. (1997). Cluster—Science and mission overview. In C. P. Escoubet, C. T. Russell, & R. Schmidt (Eds.), *The cluster and phoenix missions*. Dordrecht: Springer. https://doi.org/10.1007/978-94-011-5666-0_1

Ferradas, C. P., Zhang, J. C., Kistler, L. M., & Spence, H. E. (2015). Heavy-ion dominance near Cluster perigees. *Journal of Geophysical Research: Space Physics*, *120*, 10485–10505. https://doi.org/10.1002/2015JA021063

Ferradas, C. P., Zhang, J. C., Spence, H. E., Kistler, L. M., Larsen, B. A., Reeves, G., & Funsten, H. (2016a). Drift paths of ions composing multiple-nose spectral structures near the inner edge of the plasma sheet. *Geophysical Research Letters*, *43*, 11484–11492. https://doi.org/10.1002/2016GL071359

Ferradas, C. P., Zhang, J. C., Spence, H. E., Kistler, L. M., Larsen, B. A., Reeves, G., & Funsten, H. (2016b). Ion nose spectral structures observed by the Van Allen Probes. *Journal of Geophysical Research: Space Physics*, *121*, 12025–12046. https://doi.org/10.1002/2016JA022942

Funsten, H. O., Skoug, R. M., Guthrie, A. A., MacDonald, E. A., Baldonado, J. R., Harper, R. W., et al. (2013). Helium, Oxygen, Proton, and Electron (HOPE) mass spectrometer for the radiation belt storm probes mission. *Space Science Review*, *179*, 423–484. https://doi.org/10.1007/s11214-013-9968-7

Ganushkina, N. Y., Pulkkinen, T. I., Bashkirov, V. F., Baker, D. N., & Li, X. (2001). Formation of intense nose structures. *Geophysical Research Letters*, *28*, 491–494. https://doi.org/10.1029/2000GL011955

Goldstein, J., Angelopoulos, V., De Pascuale, S., Funsten, H. O., Kurth, W. S., LLera, K., & Wygant, J. R. (2017). Cross-scale observations of the 2015 St. Patrick's day storm: THEMIS, Van Allen Probes, and TWINS. *Journal of Geophysical Research: Space Physics*, *122*, 368–392. https://doi.org/10.1002/2016JA023173

Goldstein, J., & McComas, D. J. (2013). Five years of stereo magnetospheric imaging by TWINS. *Space Science Review*, *180*, 39–70. https://doi.org/10.1007/s11214-013-0012-8

Goldstein, J., Pascuale, S. D., Kletzing, C., Kurth, W., Genestreti, K. J., Skoug, R. M., & Spence, H. (2014). Simulation of Van Allen probes plasmapause encounters. *Journal of Geophysical Research: Space Physics*, *119*, 7464–7484. https://doi.org/10.1002/2014JA020252

Grimes, E. W., Perez, J. D., Goldstein, J., McComas, D. J., Valek, P., & Turner, D. (2013). Comparison of TWINS and THEMIS observations of proton pitch angle distributions in the ring current during the 29 May 2010 geomagnetic storm. *Journal of Geophysical Research: Space Physics*, *118*, 5454–5466. https://doi.org/10.1002/jgra.50455

Henderson, M. G., Reeves, G. D., Spence, H. E., Sheldon, R. B., Jorgensen, A. M., Blake, J. B., & Fennell, J. F. (1997). First energetic neutral atom images from Polar. *Geophysical Research Letters*, *24*, 1167–1170. https://doi.org/10.1029/97GL01162

Jaggi, R. K., & Wolf, R. A. (1973). Self-consistent calculation of the motion of a sheet of ions in the magnetosphere. *Journal of Geophysical Research*, *78*(16), 2852–2866. https://doi.org/10.1029/JA078i016p02852

Kovrazhkin, R. A., Sauvaud, J. A., & Delcourt, D. C. (1999). INTERBALL-Auroral observations of 0.1–12 keV ion gaps in the diffuse auroral zone. *Annales Geophysicae*, *17*, 734–742. https://doi.org/10.1007/s00585-999-0734-9

Lennartsson, W., Shelley, E. G., Sharp, R. D., Johnson, R. G., & Balsiger, H. (1979). Some initial ISEE-1 results on the ring current composition and dynamics during the magnetic storm of December 11, 1977. *Geophysical Research Letters*, *6*, 483–486. https://doi.org/10.1029/GL006i006p00483

Li, X., Baker, D. N., Temerin, M., Peterson, W. K., & Fennell, J. F. (2000). Multiple discrete-energy ion features in the inner magnetosphere: Observations and simulations. *Geophysical Research Letters*, *27*, 1477–1450. https://doi.org/10.1029/1999GL010745

Li, S. Y., Luo, H., Kronberg, E. A., Ferradas, C. P., Du, A. M., Ge, Y. S., & Deng, H. (2020). Stationary "nose-like" ion spectral structures in the inner magnetosphere: Observations by Van Allen probes and simulations. *Journal of Atmospheric and Solar-Terrestrial Physics*, *211*, 105390.

Lundin, R., Lyons, L. R., & Pissarenko, N. (1980). Observations of the ring current composition at L < 4. *Geophysical Research Letters*, *7*, 425–428. https://doi.org/10.1029/GL007i006p00425

McComas, D. J., Allegrini, F., Baldonado, J., Blake, B., Brandt, P. C., Burch, J., & Zoennchen, J. (2009). The two wide-angle imaging neutral-atom spectrometers (TWINS) NASA mission-of-opportunity. *Space Science Reviews*, *142*, 157–231. https://doi.org/10.1007/s11214-008-9467-4

McFadden, J.P., Carlson, C.W., Larson, D., Ludlam, M., Abiad, R., Elliott, B., & Angelopoulos, V. (2008). The THEMIS ESA plasma instrument and in-flight calibration. *Space Science Reviews*, *141*, 277–302. https://doi.org/10.1007/s11214-008-9440-2

Mitchell, D. G., Jaskulek, S. E., Schlemm, C. E., Keath, E. P., Thompson, R. E., Tossman, B. E., & Powell, F. R. (2000). High energy neutral atom (HENA) imager for the image mission. In J. L. Burch (Eds.), *The image mission*. Dordrecht: Springer. https://doi.org/10.1007/978-94-011-4233-5_4

Mitchell, D. G., Son Brandt, P. C., Roelof, E. C., Hamilton, D. C., Retterer, K. C., & Mende, S. (2003). Global imaging of O+ from IMAGE/HENA. *Space Science Reviews*, *109*, 63–75. https://doi.org/10.1023/B:SPAC.0000007513.55076.00

Perez, J. D., Goldstein, J., McComas, D. J., Valek, P., Buzulukova, N., Fok, M. C., & Singer, H. J. (2015). TWINS stereoscopic imaging of multiple peaks in the ring current. *Journal of Geophysical Research: Space Physics*, *120*, 368–383. https://doi.org/10.1002/2014JA020662

Perez, J. D., Goldstein, J., McComas, D. J., Valek, P., Fok, M. C., & Hwang, K. J. (2016). Global images of trapped ring current ions during main phase of 17 March 2015 geomagnetic storm as observed by TWINS. *Journal of Geophysical Research: Space Physics*, *121*, 6509–6525. https://doi.org/10.1002/2016JA022375

Perez, J. D., Grimes, E. W., Goldstein, J., McComas, D. J., Valek, P., & Billor, N. (2012). Evolution of CIR storm on 22 July 2009. *Journal of Geophysical Research*, *117*, A09221. https://doi.org/10.1029/2012JA017572

Peterson, W. K., Trattner, K. J., Lennartsson, O. W., Collin, H. L., Baker, D. N., Pulkkinen, T. I., & Roeder, J. L. (1998). *Imaging the plasma sheet with energetic ions from the POLAR satellite*, Japan: International Conference on Substorms-4. https://doi.org/10.1007/978-94-011-4798-9_169

Roelof, E. C. (1987). Energetic neutral atom image of a storm-time ring current. *Geophysical Research Letters*, *14*, 652–655. https://doi.org/10.1029/GL014i006p00652

Roelof, E. C. (1997). ENA emission from nearly-mirroring magnetospheric ions interacting with the exosphere. *Advances in Space Research*, *20*(3), 361–366. https://doi.org/10.1016/S0273-1177(97)00692-3

Shirai, H., Maezawa, K., Fujimoto, M., Mukai, T., Saito, Y., & Kaya, N. (1997). Mono energetic ion drop-off in the inner maghetosphere. *Journal of Geophysical Research, 102*, 19873–19882. https://doi.org/10.1029/97JA01150

Smith, P. H., & Hoffman, R. A. (1974). Direct observations in the dusk hours of the characteristics of the storm time ring current particles during the beginning of magnetic storms. *Journal of Geophysical Research*, *79*, 966–971. https://doi.org/10.1029/JA079i007p00966

Valek, P., Brandt, P. C., Buzulukova, N., Fok, M. C., Goldstein, J., McComas, D. J., & Skoug, R. (2010). Evolution of low-altitude and ring current ENA emissions from a moderate magnetospheric storm: Continuous and simultaneous Twins observations. *Journal of Geophysical Research*, *115*, A11209. https://doi.org/10.1029/2010JA015429

Valek, P. W., Delmonico, E., McComas, D. J., Goldstein, J., Allegrini, F., & Livi, S. (2018). Composition of 1–128 keV Magnetospheric ENAs. *Journal of Geophysical Research: Space Physics*, *123*, 2668–2678. https://doi.org/10.1002/2017JA024997

Valek, P. W., Goldstein, J., Jahn, J. M., McComas, D. J., & Spence, H. E. (2015). First joint in situ and global observations of the medium-energy oxygen and hydrogen in the inner magnetosphere. *Journal of Geophysical Research: Space Physics*, *120*, 7615–7628. https://doi.org/10.1002/2015JA021151

Valek, P. W., Goldstein, J., McComas, D. J., Iiie, R., Buzulukova, N., Fok, M. C., & Perez, J. D. (2013). Oxygen-hydrogen differentiated observations from TWINS: The 22 July 2009 storm. *Journal of Geophysical Research: Space Physics*, *118*, 3377–3393. https://doi.org/10.1002/jgra.50204

Vallat, C., Dandouras, I., Brandt, P. C., DeMajistre, R., Mitchell, D. G., Roelof, E. C., & Balogh, A. (2004). First comparisons of local ion measurements in the inner magnetosphere with energetic neutral atom magnetospheric image inversions: Cluster-CIS and IMAGE-HENA observations. *Journal of Geophysical Research*, *109*, A04213. https://doi.org/10.1029/2003JA010224

Vallat, C., Ganushkina, N., Dandouras, I., Escoubet, C. P., Taylor, M. G., Laakso, H., & Daly, P. (2007). Ion multi-nose structures observed by Cluster in the inner Magnetosphere. *Annales Geophysicae*, *25*, 171–190. https://doi.org/10.5194/angeo-25-171-2007

Wahba, G. (1990). *Spline models for observational data*, SIAM: CBMS-NSF Regional Conference Series in Applied Mathematics. https://doi.org/10.1137/1.9781611970128

Zhang, J. C., Kistler, L. M., Spence, H. E., Wolf, R. A., Reeves, G., Skoug, R., & Luo, H. (2015). Trunk-like" heavy ion structures observed by the Van Allen Probes. *Journal of Geophysical Research: Space Physics*, *120*, 8738–8748. https://doi.org/10.1002/2015JA021822

Zhao, H., Baker, D. N., Califf, S., Li, X., Jaynes, A. N., Leonard, T., & Spence, H. E. (2017). Van Allen probes measurements of energetic particle deep penetration into the low L Region (L < 4) during the storm on 8 April 2016. *Journal of Geophysical Research: Space Physics*, *122*, 12140–12152. https://doi.org/10.1002/2017JA024558